Astronomy & Astrophysics

Albedo–color distribution on Mercury

A photometric study of the poorly known hemisphere

J. Warell and P.-G. Valegård

Institutionen för Astronomi och Rymdfysik, Uppsala Universitet, Box 515, 751 20 Uppsala, Sweden
e-mail: johan.warell@astro.uu.se

ABSTRACT

Aims. The variation of albedo and color of Mercury's surface is studied with disk-resolved image data obtained at six evenly spaced wavelengths in the optical to near infrared wavelength range (447–944 nm) with the 1-m Swedish Solar Telescope on La Palma in April, 2003.

Methods. Disk images have been modeled and photometrically normalized with the light scattering theory of Hapke to derive albedo–color properties of a poorly known region (unimaged by Mariner 10) of Mercury's surface between longitudes 210°W and 270°W. Maps of relative abundances of ferrous iron, titanium and optical maturation are derived on the basis of a feldspathic model for the crustal composition and previous results for the Moon, assuming the validity of the general maturation model for mafic silicate regoliths of atmosphereless bodies.

Results. The albedo–color scatterplot distributions of Mercury's surface are uniform with respect to wavelength in the near-ultraviolet to near-infrared due to the absence of strong absorption bands in the reflectance spectrum. The extents of the distributions are less than for the global Moon and similar to that of the lunar farside, which is related to the relatively subdued color contrasts of Mercury's primarily feldspathic surface. At the attained 500-km spatial resolution scale, these maps do not indicate the existence of surface regions chemically similar to the lunar maria, which have a high FeO and TiO$_2$ content. Variations in abundances of ferrous iron and titanium are shown to be less than for the global Moon and similar to the lunar farside at the same spatial scale. Optically bright regions on Mercury are less mature and less opaque than their surroundings consistent with geologically recent immature crater ejecta, while localized dark regions generally have intermediate maturities and iron abundances and higher-than-average titanium abundances. The smaller relative intensity range of spatial variations of spectral parameters in the near infrared compared to the near ultraviolet may imply that relative abundance variations in ferrous iron are smaller than variations in opaque minerals.

Conclusions. The results reinforce the similar natures of the Mariner 10-imaged and the poorly known hemispheres of Mercury, as well as their superficial similarity to the lunar farside, and demonstrate that geological interpretation of ground-based observations of albedo features on Mercury is possible.

Key words. planets and satellites: individual: Mercury – Moon

1. Introduction

The spectral properties of the regolith of an atmosphereless mafic silicate body are governed by three major components (Hapke et al. 1975; Rava & Hapke 1987): 1) ferrous iron as FeO in mafic minerals and glasses, the increased abundance of which increases the depth of the near-infrared crystal field absorption band, 2) nm-sized nanophase metallic iron (npFe) particles formed by vapor deposition reduction in rims of mafic grains, the increased presence of which increases the slope of the spectrum ("spectral reddening") and decreases the reflectance, and 3) spectrally neutral Ti-rich opaque phases such as ilmenite in minerals and glasses, the increased abundance of which decreases the reflectance but decreases the spectral slope. Various transition elements such as Ti present in the silicate matrix of mafic minerals cause an oxygen-metal charge transfer absorption feature almost invariably seen in mafic mineral spectra, and which reddens the spectrum at wavelengths shorter than about 550 nm. This near-UV band has not been clearly detected on Mercury, likely due to the strongly matured surface.

About 60% of the abundance of metallic iron in the lunar regolith is likely contributed by the original crust and meteorite impacts, the remainder being produced by vapor deposition reduction of FeO (Morris 1980). The nanophase metallic iron is formed during the maturation process due to micrometeorite impacts and solar wind sputtering of the surface, leading to condensation of Fe-bearing silicate vapors in silicate grain rims by selective loss of oxygen (Hapke et al. 1975; Hapke 2001, and references therein). Metallic iron is present in greater abundance in the bulk of the smallest size fraction of lunar soils, indicating that their formation is predominantly a surface-related phenomenon (Pieters et al. 2000; Noble et al. 2001; Taylor et al. 2001). Their predicted presence in lunar soil grain surfaces (Cassidy & Hapke 1975) was first observed by Keller & McKay (1997). Realistic pulse laser irradiation experiments carried out by Sasaki et al. (2003) on olivine and pyroxene samples with 8–10 wt% FeO have simulated the putative production of npFe by micrometeorites, who predict that such processes should occur at lower FeO abundances of 3–5%, similar to the ferrous iron abundance of Mercury's surface.

The optical spectrum of Mercury was modeled by Warell & Blewett (2004) with the light scattering theory of Hapke (2001) to obtain quantitative information on the iron chemistry. They proposed that very small amounts of npFe (0.1–0.3 wt%) in coatings of approximately 30 μm-sized grains can explain the strong red slope and absence of absorption bands in Mercury's spectrum. This amount of npFe may be provided by a predominantly

feldspathic mineralogy containing <3% FeO in iron-poor pyroxenes, or alternatively be provided by meteoritic sources (Noble & Pieters 2003).

Increasing abundance of npFe particles in the surfaces of soil grains cause a reddening of the visible part of the spectrum of a mafic mineral, followed by a reddening of the entire continuum up to near-infrared wavelengths as abundances as increased (Pieters et al. 2000). During the processing of regolith material by energetic impacts, matured grains are shattered, vaporized, melted and fused. This leads to the formation of larger complex glass-rich agglutinates in which the npFe is distributed more evenly throughout the volume than is the case in individual grains. The general optical effect of agglutinates is to darken the visible spectrum, and is directly related to the mass fraction of npFe present in a semitransparent matrix (Hapke 2001). Agglutinates alone cannot account for all of the observed optical alteration of lunar soils, and though they are abundant in mature soils, they are not the principal carrier of maturation effects (Pieters et al. 1993). Agglutinates are the result of melting of the finest size fractions of the soil and as such acquire more npFe as time proceeds, if there is sufficient FeO available for reduction in the source material.

In the maturation model of Rava & Hapke (1987), the effects on the spectrum of npFe and neutral opaque phases are complementary in terms of reflectance but competitive in terms of color. This enabled Robinson & Lucey (1997) to decompose their spectral effects on the regolith of Mercury through the shape of the distribution of scatterplots in the ultraviolet–visible (UVVIS) albedo – color space formed by the 575 nm albedo and 355 nm/575 nm albedo ratio ("color") derived from Mariner 10 images. Recently, Blewett et al. (2005) used the same data set to study the albedo–color distribution of the Mariner 10 first encounter data for longitudes 10°W–90°W.

In this paper, we perform an albedo–color analysis of a previously uncharacterized surface region on the poorly known hemisphere. The methods are similar to those of Robinson & Lucey (1997) and Blewett et al. (2005) and are based on the methods of Lucey et al. (2000). We include also visual–near infrared (VISNIR) images to clearly separate spectral effects of optical maturity from those of ferrous iron, which is not possible in the UVVIS. Our Earth-based data covers the longitude range 210°W–270°W of Mercury, unimaged by Mariner 10. We compare the poorly known and Mariner 10 hemispheres with each other in albedo–color and geochemical sense, and with the properties of the Moon.

2. Observations and data reduction

The observations selected for the present analysis were made in the daytime on April 14, 2003, during an eastern elongation of Mercury. We used the 1-m Swedish Solar Telescope (SST; Scharmer et al. 2002) on La Palma for CCD imaging observations with 36–63 nm bandpass Ealing interference filters centered at 447, 554, 650, 753, 833 and 944 nm. A UV-sensitive Kodak MegaPlus 4.2i camera with a KAF-4202 chip (pixel size 9×9 μm, 2029×2044 pixel array, 10-bit digitization) was used at the secondary $f/45$ focus employed for solar observations, providing an image scale of 0.041″/pixel. Exposure times in the range 0.4 to 1.0 second were required to attain adequate signal-to-noise ratio (SNR) for individual images. Though the adaptive optics system was not operating, the benefits of an unobstructed and diffraction-limited optical system, corrected for achromatic aberration and atmospheric dispersion, could still be utilized.
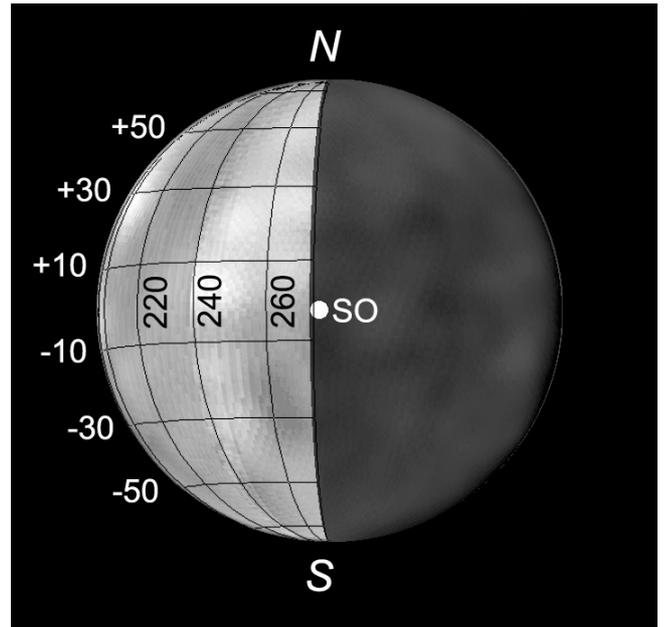

Fig. 1. Photometrically normalized brightness variation across the apparent disk of Mercury for April 14, 2003. The map has N up and is labelled by western longitude and latitude at 20° grid spacing. The sub-observer point is marked "SO". This hemisphere of Mercury, unimaged by Mariner 10, is dominated by the following optically bright albedo features (also labelled in Fig. 4A), identified as in Warell & Limaye (2001) and from which the base map is taken: SVST ID #52 at (242°W, +10°), #53 (244°W, −8°), #54 (245°W, −24°), #55 (254°W, +24°), and #56 (265°W, +16°). The classical dark feature Solitudo Criophori ("SC") is located on the terminator at (260°W, −1°). Other local dark features are "A" (245°W, −50°), "B" (262°W, −25°) and "C" (225°W, 0°).

At the time of the observations, Mercury was located 19.6° east of the Sun at a phase angle of 95.0°. The 46% illuminated disk was 7.3″ in diameter and had a visual magnitude of −0.1. The sub-observer longitude and latitude were 276°W and −3°, with a sub-solar longitude of 181°W. The longitude range of the illuminated and visible disk was 186°W–271°W (Fig. 1), which is just west of the half-hemisphere imaged by Mariner 10. During the observations, Mercury descended from altitude 60° to 49°, corresponding to an air mass of 1.1 to 1.3. The sky was mostly clear with some scattered cirrus and excellent transparency.

2.1. Data reduction

Selected high contrast images were individually processed with median-filtered master flat, dark and bias frames obtained the same day. 6–11 of the sharpest images in each color were then sub-pixel aligned, rotated and stacked using median averaging of pixel values, to produce single master images of high signal-to-noise ratio (SNR 220–1600) for each filter. A constant value was subtracted from all master image pixels such that the average intensity of the background sky was set to zero. Bicubic interpolation resampling was then applied to obtain master images for each filter with disk diameters of 35 pixels (corresponding to pixel scale of 0.21″ or 140 km/pixel at Mercury's distance) to further increase the SNR, more optimally sample the image scale with respect to seeing, and reduce computational time for the subsequent photometric modeling.

Table 1. Hapke parameters of the modeled Mercury image data as a function of wavelength λ. The initial model is that of Warell (2004) Sol. 1 for the V band. Parameter ranges used while iteratively finding the best solutions are given.

λ (nm)	w	b	c	h	B_0	$\bar{\theta}$ (°)
Initial	0.16	0.18	1.1	0.09	2.7	8
Range	0.1–0.4	0.16–0.20	0.9–1.3	Fixed	Fixed	0–40
447	0.14	0.18	1.1	0.09	2.7	20
554	0.18	0.18	1.1	0.09	2.7	20
650	0.22	0.18	1.1	0.09	2.7	20
753	0.26	0.18	1.1	0.09	2.7	20
833	0.28	0.18	1.1	0.09	2.7	20
944	0.32	0.18	1.1	0.09	2.7	20

2.2. Data modeling

To obtain an intensity calibration, the total intensity of the observed 553 nm disk image was scaled to the total radiance factor value of the modeled apparent disk for the same wavelength and pixel sampling, calculated using the photometric model of Hapke (2002). The parameters of "Solution 1" of Warell (2004) for the V band ($w = 0.16$, $b = 0.18$, $c = 1.1$, $h = 0.09$, $B_0 = 2.7$, $\bar{\theta} = 8°$), derived from the integrated V-band phase curve for the phase angle range $3°$–$170°$ (Mallama et al. 2002), were used as a starting point for the iterations. The total observed disk intensities at other wavelengths were scaled relative to the V-band according to the slope of Mercury's reflectance spectrum for standard photometric geometry (Warell & Blewett 2004). Following this operation, each master image disk pixel contained the seeing-convolved value of the radiance factor for the corresponding wavelength and location on Mercury. The seeing-convolved value is the intensity obtained when setting the total disk intensity to the sum of the radiance factor for all Hapke model disk pixels for the corresponding wavelength.

Following intensity calibration the two-dimensional photometric function across the disk, caused by variations in the observational geometry, was modeled for each observed disk. The Hapke (2002) model was employed with boundary conditions imposed by the total brightness of the disk at each wavelength, and the expected wavelength-independent value of $\bar{\theta}$ (Domingue & Hapke 1989). The best-fit model for each wavelength was found in an iterative search in multi-dimensional parameter space (Table 1), with parameter values centered on those for Solution 1 of Warell (2004). The following ranges were employed: $w = 0.1$–0.4, $b = 0.16$–0.20, $c = 0.9$–1.3, $\bar{\theta} = 0°$–$40°$, while h and B_0 were held constant at 0.09 and 2.7, respectively, as their values are not possible to determine at the present phase angle. Among determinations of h and B_0 by various researchers (Bowell et al. 1989; Domingue et al. 1997; Mallama et al. 2002; Veverka et al. 1988; Warell 2004) there is general consensus that these values are near 0.09 and 2.5, respectively, while for the other parameters the modeling results vary substantially. Variations in b and c have little influence on the phase curve brightness at phase angles near $90°$ and no significant variations from the initial values were found. The parameters which are of greatest importance for the disk brightness are w and $\bar{\theta}$ motivating that their ranges were generous in the present study.

During modeling, the calculated Hapke disk models were convolved with the proper Gaussian seeing point spread function (PSF), prior to comparison with the intensity calibrated master image (in the following referred to as "observation"). The full width at half maximum (FWHM) of the PSF corresponded to nearly $1.0''$ or $\sim$500 km on mid-disk. The best-fit model for

each wavelength was determined from the root-mean-square difference between observation and seeing convolved model on a pixel-by-pixel basis. The best fit models were found to have a surface roughness value of $20°$, and a particle single scattering albedo of 0.14 to 0.32 for the range 447 to 944 nm. This is similar to the determination of other authors for the average surface of Mercury on spatial scales greater than local or regional. Emery et al. (1998) found a surface roughness parameter of $20°$, Mallama et al. (2002) found $16°$, while Sprague et al. (2000) found smaller values in the range 8–$11°$. The value of $8°$ determined by Warell (2004) is heavily influenced by the intensity of the V-band phase curve at high phase angles; for observations at $\alpha > 165°$ (Mallama et al. 2002), the phase curve brightness is contributed to a major extent by local smooth plains units near the northern pole, and a model with a smooth surface provides the best fit to the observations.

Following the determination of the best-fit seeing-convolved disk models, the observations were divided by the models to obtain photometrically normalized surface brightness distributions. To compare the derived albedo–color diagrams for Mercury with those for the Moon, the average brightness of the photometrically normalized 553 nm image was scaled to the V-band geometric albedo of 0.136 derived from the Hapke parameter set of Solution 1 of Warell (2004), taking into account information of the complete phase curve. The precision of this value, derived from the error in the model fit itself, is estimated to 4% and encompasses the range determined recently by other authors (Mallama et al. 2002; Veverka et al. 1988) from different phase curve data. The 447 nm, 753 nm and 944 nm albedo images were then scaled in intensity to form albedo images at 415 nm, 750 nm and 950 nm, respectively, using the observed spectral slope and albedo of Mercury at standard photometric geometry (Warell & Blewett 2004).

The Clementine image intensities were then scaled with the V-band geometric albedo of 0.152 derived from the Hapke parameter set of solution 4 of Warell (2004), which includes information from the complete integral phase curve. The albedos at the Clementine wavelengths were derived by scaling their intensities relative to the V-band albedo using reflectance values for a region in Mare Serenitatis (Lucey et al. 2000a). This procedure circumvents any possible calibration errors related to the Clementine data set (Hillier 1999; Shkuratov et al. 2002; see also Sect. 5), and puts the lunar and mercurian data sets on the same wavelength and albedo scale.

In order to study color variations across the mercurian surface and perform an analysis according to the methods of Lucey at al. (2000a,b), the photometrically normalized images were divided with the 750 nm albedo image, producing the image ratios (colors) $I(415)/I(750)$, and $I(950)/I(750)$. Albedo–color data for $\sim$250 disk pixels not affected by limb defects were extracted at each wavelength and used in the analysis. Figures 4C and 5A show the resulting ratio images.

3. Data analysis

The derived UVVIS and VISNIR albedo–color distributions derived from 415 nm, 750 nm and 950 nm data for Mercury are compared with those of the Moon in Figs. 2 and 3. For Mercury, there is no significant variation with wavelength in the shape of the scatterplot distribution across the optical–near infrared range, due to the absence of prominent absorption bands. The lunar data set is based on calibrated Clementine data at 450 and 750 nm for the whole Moon between latitudes $-70°$ and $+70°$, at a nominal scale of $1°$/pixel (Eliason et al. 1999; Isbell et al. 1999;
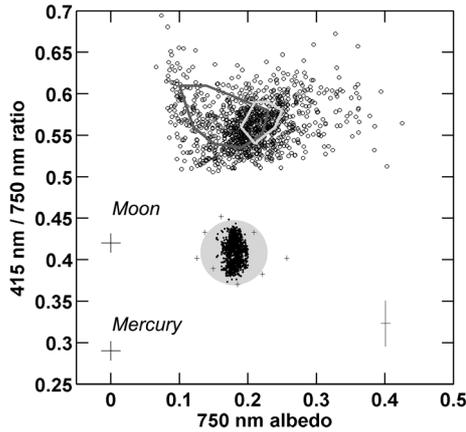
Fig. 2. The distributions of the 750 nm albedo versus 415 nm/750 nm reflectance ratio of Mercury (*bottom*) and the global Moon (*top*). The scatterplot for Mercury (filled dots) is the observed distribution for the longitude range 210°W–270°W, the shaded ellipse represents the derived true extent of the distribution, and the crosses depict the result of Blewett et al. (2005) from Mariner 10 data for longitudes 10°W–70°W. Errorbars for the observed Mercury data are shown in the lower right corner. The lunar scatterplot (circles) is derived from Clementine images of the whole lunar surface between latitudes -70° and +70°. The region enclosed by a dark grey line defines the simulated distribution of the global Moon under Mercury observation conditions (to be compared with the region of filled dots for Mercury), while the smaller light grey line shows the corresponding envelope for the lunar farside. The cross mark to the lower left of the lunar distribution is located at the point (0.00, 0.42) used by Lucey and coworkers as the origin in the derivation of the Ti-sensitive parameter θ_{Ti} (Lucey et al. 2000a). The cross mark at the lower left of the mercurian distribution at coordinates (0.00, 0.29) is the corresponding origin used here for calculating the Ti-sensitive and the iron-maturity sensitive parameters for Mercury.

Fig. 3. The distributions of the 750 nm albedo versus 950 nm/750 nm reflectance ratio of Mercury (*top*) and the global Moon (*bottom*). The scatterplot for Mercury (filled dots) is the observed distribution for the longitude range 210°W–270°W. The lunar scatterplot (circles) is derived from Clementine images of the whole lunar surface between latitudes −70° and +70°. The region enclosed by a dark grey line defines the simulated distribution of the global Moon under Mercury observation conditions, while the smaller light grey line shows the corresponding envelope for the lunar farside. The cross mark to the upper left of the lunar distribution is located at the point (0.08, 1.19) used by Lucey and coworkers as the origin in the derivation of the Fe-sensitive parameter θ_{Fe} (Lucey et al. 2000a) and the optical maturity parameter OMAT (Lucey et al. 2000b). The cross mark at the upper left of the mercurian distribution at coordinates (0.06, 1.37) is the corresponding origin used here for calculating the Fe-sensitive and optical maturity sensitive parameters for Mercury. Errorbars for Mercury are similar to those of Fig. 2.

Robinson et al. 1999, obtained via the Planetary Data System). It has been sampled with the same relative pixel scale as the Mercury observations to obtain an equal number of points across the disks and in the scatterplots for the two bodies.

3.1. Correction for seeing smear

Seeing smear will reduce the range of data in both the albedo and color axes, independently of observational sampling. To simulate this effect, the lunar data set was convolved with a Gaussian PSF of appropriate width and Poisson noise added, followed by resampling to obtain a spatial resolution, image quality and number of data points equivalent to that of the Mercury observations. With increased Gaussian smoothing, the parameter range in terms of albedo and color decreases, neighboring pixel intensities become more strongly correlated, detail is blurred and extreme data poitns are effectively removed.

In Fig. 2, the resulting UVVIS (750 nm versus 415/750 nm) distribution for the convolved global lunar surface does not preserve the orthogonal highland and mare trends present in the nominal data set. It becomes rotated and its center slightly shifted in location, and a broad extension is apparent in the direction of the nominal mare trend. In the present case, a Gaussian seeing PSF with FWHM of the order of 1/7th of the apparent disk (as for the Mercury observations) applied to a body with the reflectance characteristics of the Moon has a strong averaging effect on the individual color trends of the mare and highland units, though the mare trend is still noticeable. The observed distribution for Mercury is more strongly concentrated than that for the nominal Moon, due to the seeing convolution
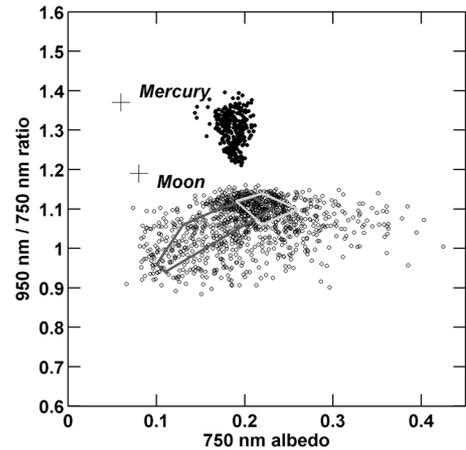
effect. Furthermore, it is smaller than the simulated global lunar distribution for the mercurian observational circumstances, but of comparable size to the convolved distribution for the lunar farside.

In Fig. 3, the resulting VISNIR (750 nm versus 950/750 nm) distribution for the global Moon is similarly reduced in extent and slightly shifted in location following convolution. The convolved distribution for the lunar farside is centered on the major concentration of points in the scatterplot for the unconvolved global Moon, and is comparable in extent to the distribution observed for Mercury.

We have estimated the extent of the true UVVIS scatterplot distribution for Mercury, corrected for seeing smear, sampling effects, and detector noise, based on the relative extents of Clementine global lunar data before and after convolution. The shaded ellipse in Fig. 2 encompassing the Mercury scatterplot shows the calculated extent of the true albedo–color distribution for the observed hemisphere of Mercury. The extent of this estimated region is comparable with the region outlined by crosses, which represents the mercurian 575 nm albedo – 355/575 nm ratio distribution of Blewett et al. (2005), which has been scaled to the plotted 750 nm versus 415/750 nm space based on the slope of the mercurian spectrum at standard photometric geometry (Warell & Blewett 2004). Blewett et al. (2005) used Mariner 10 incoming hemisphere data in their analysis.

3.2. Mapping relative chemical abundances

The determination of TiO_2 and FeO concentrations in the lunar crust was initialized by Charette et al. (1974) and Charette et al. (1977), respectively. In a series of papers finalized in

Lucey et al. (2000a), more sophisticated methods were developed to derive maps of the abundance of titanium and iron and the degree of maturation of the lunar surface, based on return sample chemical abundance determinations and Clementine multispectral imaging of the sample sites. The similar natures of the mercurian and lunar surfaces and the assumption that space weathering proceeds similarly on the two bodies as their surfaces are dominated by mafic silicate minerals and rock types (e.g., Dollfus & Auriere 1974; Rava & Hapke 1987; Cintala 1992; Blewett et al. 1997; Hapke 2001; Sprague et al. 2002; Warell & Blewett 2004), enables these methods to be transferred to Mercury. Though absolute abundances are not possible to determine accurately for Mercury due to the lack of available surface samples with which to calibrate remote-sensing data, relative intensities or colors of geologic units were first used by Robinson & Lucey (1997) to estimate relative iron-plus-maturity and opaque Ti-rich mineral abundances from Mariner 10 data.

Following the aforementioned methods, we have used the present UVVIS data set for a region of Mercury previously uninvestigated in this respect to map four spectral parameters: 1) the relative abundance of Ti-rich opaque minerals, and 2) the combined maturity and abundance of ferrous iron. These results are comparable to the work of Robinson & Lucey (1997). We have used our VISNIR data set to map 3) the relative abundance of iron and 4) the relative degree of optical maturity. Note that the spectral effects of ferrous iron is separable from the effects of optical maturity (nanophase metallic iron) in the VISNIR, which is not the case in the UVVIS.

3.3. Titanium mapping

The method of titanium mapping relies on the assumption that structure in the VIS reflectance versus UV/VIS reflectance ratio is directly correlated to the TiO_2 content and iron-plus-maturity of the surface.

Lucey et al. (1998) formulate a titanium-sensitive parameter,

$$\theta_{Ti} = \arctan\left(\frac{R_{415}/R_{750} - y_{0Ti}}{R_{750} - x_{0Ti}}\right) \tag{1}$$

which is the angle between the horizontal and the line from the origin at (x_{0Ti}, y_{0Ti}) to the data point at $(R_{750}, R_{415}/R_{750})$ in the UVVIS diagram. x_{0Ti} is the 750 nm reflectance at the origin and y_{0Ti} is the R_{415}/R_{750} ratio value at the origin. The angle θ_{Ti} is directly related to the abundance of TiO_2, with a higher value indicating a greater abundance of Ti-rich opaque minerals. We form a parameter FeOMAT, the iron-plus-maturity parameter,

$$\text{FeOMAT} = \sqrt{(R_{750} - x_{0Ti})^2 + \left(\frac{R_{415}}{R_{750}} - y_{0Ti}\right)^2}, \tag{2}$$

represented by the Euclidean distance from the origin to the data point and whose trend is approximately orthogonal to θ_{Ti} in the UVVIS diagram. High values correspond to lower abundance of iron and/or higher maturity. Points in the UVVIS diagram lying along a line with the same value of θ_{Ti} have the same Ti concentration, but varying maturity and/or ferrous iron abundance.

3.4. Iron mapping

The method of iron mapping relies on the assumption that structure in the VIS reflectance versus NIR/VIS reflectance ratio is directly correlated to the FeO content and degree of maturity.

We use the iron-sensitive parameter of Lucey et al. (2000a) to map the relative abundance of ferrous iron in the surface,

$$\theta_{Fe} = \arctan\left(\frac{R_{950}/R_{750} - y_{0Fe}}{R_{750} - x_{0Fe}}\right) \tag{3}$$

which is the angle between the horizontal and the line from the origin at (x_{0fe}, y_{0Fe}) to the data point $(R_{750}, R_{950}/R_{750})$ in the VISNIR diagram. Higher values of θ_{Fe} correspond to greater FeO abundance. The OMAT parameter (Lucey et al. 2000b), sensitive to degree of optical maturity, is

$$\text{OMAT} = \sqrt{(R_{750} - x_{0Fe})^2 + \left(\frac{R_{950}}{R_{750}} - y_{0Fe}\right)^2}, \tag{4}$$

and trends roughly orthogonally to θ_{Fe}; it is represented by the Euclidean distance from the origin to the data point. A large OMAT value indicates a low degree of optical maturity.

3.5. Application of lunar chemical mapping methods to Mercury

The origin $(x_{0Ti}, y_{0Ti}) = (0.00, 0.42)$ was determined by Lucey et al. (2000a) from a least squares fit between measured θ_{Ti} values for lunar sample sites and TiO_2 abundance values for lunar return samples. It is located at the point of convergence of trends for lunar samples with constant TiO_2 abundance but varying maturity. Similarly, the origin $(x_{0Fe}, y_{0Fe}) = (0.08, 1.19)$ was determined by Lucey et al. (2000a) from a least squares fit between measured θ_{Fe} and FeO abundance values. This origin corresponds to the location of a "hypermature" red dark endmember and represents the convergence of trends for lunar samples with varying FeO abundance. The exact locations of these origins in the UVVIS and VISNIR plots is not critical as many locations produce similarly good correlations between spectra of remotely sensed lunar sites and laboratory measured chemical properties (Lucey et al. 2000a).

Given the lack of samples from Mercury's surface, we cannot derive quantitative abundances of iron, titanium or degree of optical maturity with the Lucey et al. (2002a,b) method. However, qualitative information is still possible to derive, as was done by Robinson & Lucey (1997) for the Mariner 10 incoming hemisphere. They used a rotation of the UVVIS plot to derive the spectral titanium-sensitive and iron-plus-maturity parameters from 355 nm and 575 nm image data. Transforming the albedo–color system to the titanium versus iron-plus-maturity system corresponds to a clockwise rotation of the scatterplot with an angle of approximately 35° for the Moon. The exact angle for Mercury cannot be determined without knowledge of chemical composition of surface samples, but may be similar to the Moon's assuming that the maturation process acts similarly (Rava & Hapke 1987).

We calculate the same spectral parameters as Robinson & Lucey (1997) but instead of applying a rotation we make explicit use of Eqs. (1) and (2) with an origin $(x_{0Ti}^{Me}, y_{0Ti}^{Me})$ appropriate for Mercury. We derive this origin from the known values of (x_{0Ti}, y_{0Ti}) for the Moon, and the results of the convolution study for the UVVIS Clementine data. In Fig. 2, we form a vector to the lunar origin from the center of the intersection point between the convolved envelopes of the global and farside Moon. The same vector placed at the center of the observed mercurian scatterplot ends at coordinates $(x_{0Ti}^{Me}, y_{0Ti}^{Me}) = (0.0, 0.29)$, which is the origin we choose for Mercury. The clockwise angle between this vector and the horisontal, measured at the origin, equals about 35°. In a
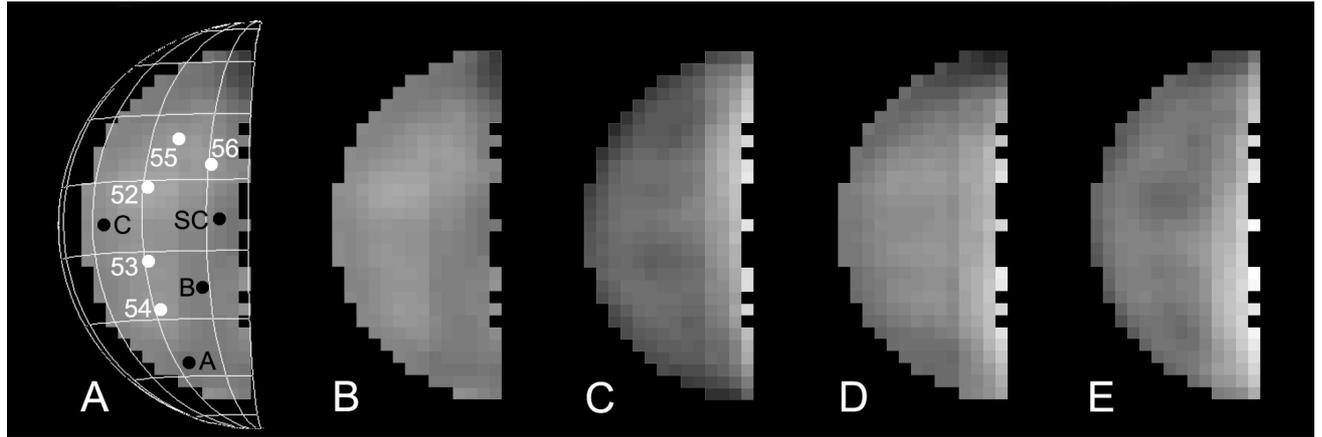
Fig. 4. Reduced UVVIS images of Mercury. Panel A shows the 750 nm albedo image with feature identifications and a coordinate grid with N at top and grid lines every 20°; the terminator longitude is 271°W, limb longitude 186°W. Optically bright features are labelled in white according to identifications in Warell & Limaye (2001), while dark features are color coded in black (refer to caption of Fig. 1 for identifications of the labelled features). The mid-disk pixel scale is 140 km. Panel B redisplays the 750 nm albedo image (range of disk-pixel values 0.17–0.22) and panel C the 415/750 nm ratio (range 0.37–0.44) which forms the basis for the derivation of the spectral parameters in the following two panels. Panel D displays the iron-plus-maturity parameter FeOMAT (brighter features are more immature and/or have lower abundances of iron; pixel range 0.17–0.30), and panel D the Ti-sensitive parameter θ_{Ti} (bright features have higher opaque mineral abundance; pixel range 0.48–0.65).

Table 2. Spectral properties of prominent features.

Feature	Coordinate	R_{750}	θ_{Ti}	FeOMAT	θ_{Fe}	OMAT
			Light features			
52	242W, +10	High	Low	High	Int.	Int.-High
53	244W, −8	Int.-High	Low-Int.	High	Low	Int.-High
54	245W, −24	High	Int.	High	Int.-High	Low-Int.
55	254W, +24	Int.-High	Low	Low	Int.	Int.
56	265W, +26	High	Int.	Int.-High	Int.-High	Low-Int.
			Dark features			
A	245W, −50	Low	Low	Low	Int.	Int.
B	262W, −25	Low-Int.	Int.-High	Int.-High	Int.	High
C	225W, 0	Low-Int.	Int.	Int.	High	Int.
SC	260W, −1	Low	Int.-High	Int.	Low-Int.	Low-Int.

similar way, we derive a new origin for Mercury in the VISNIR diagram, $(x_{0Fe}^{Me}, y_{0Fe}^{Me}) = (0.06, 1.37)$.

4. Results

Maps of the four derived spectral parameters are shown in Fig. 4D and E for the UVVIS case and in Fig. 5B and C for the VISNIR case. The spectral properties of five bright and four darker features are summarized in Table 2. In terms of the general maturation model, geologically young lunar ray craters and their ejecta have have high reflectances (high R_{750}), low titanium abundances (low θ_{Ti}), and low optical maturities (high OMAT values). More iron- and titanium-rich areas, typical for lunar maria-type surfaces, have low R_{750}, intermediate to high θ_{Ti} and high θ_{Fe}. Less iron- and titanium-rich areas, typical for lunar highland-type surfaces, have intermediate R_{750}, low θ_{Ti} and low θ_{Fe}.

In the Mercury data set, the optically bright features have properties which are generally consistent with geologically young ray craters. Darker features generally tend to have similar maturities but higher-than-average opaque and ferrous iron abundances. Due to the smearing seeing effects, spectrally extreme and extended features (e.g., #52 and #54) are expected to display less averaged properties than smaller and/or spectrally average features (e.g., B and C), which is a complicating factor in interpretation.

As Figs. 2 and 3 show, the derived true UVVIS and VISNIR albedo–color distributions for the observed hemisphere of Mercury are equantly shaped, and considerably less extended than the Moon. The UVVIS scatterplot for the global Moon shows two main trends of data: the region occupied by maria, extending from (0.10, 0.60) to (0.15, 0.53) in albedo–color space; and the approximately orthogonally directed region occupied by highlands, extending from (0.15, 0.51) to (0.27, 0.59). The global lunar UVVIS distribution for the simulated observational conditions of Mercury is greater in extent than the observed distribution for Mercury, and is elongated in the direction of the lunar mare albedo–color trend of the nominal lunar distribution. The nominal distribution for the lunar farside is basically confined to the region of the nearside highland trend due to the domination of highland terrain on this hemisphere.

The absence of trends in the observed mercurian UVVIS distribution, and the equant shape of the simulated lunar farside distribution, implies that trends in the nominal mercurian distribution are either absent or less extreme (i.e., less populated and/or less rich in color) than the case for the global Moon. Since the average mercurian surface has been determined to be spectrally similar to mature lunar highlands (Blewett et al. 1997; 2002; Warell & Blewett 2004), the conclusion drawn is that the mare trend is less developed on the observed hemisphere of Mercury than on the global Moon, and equally or less developed than on the lunar farside.

The smaller 415/750 nm and higher 950/750 nm albedo ratio values of Mercury compared to the Moon results from its average spectrum being more strongly sloped ("redder"). The somewhat lower 750 nm average albedo of Mercury implies a somewhat less reflective surface. Both these results are caused by the data being scaled according to the disk integrated mercurian spectrum at standard photometric geometry (Warell & Blewett 2004). That spectrum is essentially linear in shape throughout the VISNIR, suggesting that the broad 1-μm telluric water band absorption forest, that has contaminated many of the previously obtained Mercury spectra, has been well corrected for. Though likely not the case here, any overcorrected water band would reduce the 950 nm intensity, causing an underestimate of the 950 nm/750 nm ratio value, and an overestimate of the inferred ferrous abundance. Thus, there is a small probability that the mercurian scatterplot is located even higher than indicated in Fig. 3. This would not affect our qualitative conclusions, however.

The simulated albedo–color distributions for the farside Moon for the observation conditions of Mercury has a higher average albedo than the average Mercury, suggesting that the lunar highland regions are generally 15–20% brighter than Mercury's average surface. This is consistent with the result of Warell (2004) who concluded that the average lunar nearside surface is 7–17% brighter than Mercury, based on a comparison between the integrated V-band phase curves of the two bodies.

5. Discussion

We may compare the UVVIS albedo–color distributions of the estimated nominal distribution of the presently observed hemisphere (longitudes 210°W–270°W) with the Mariner 10 incoming hemisphere (longitudes 10°W–70°W) as derived by Blewett et al. (2005). As is seen in Fig. 2, the sizes of the distributions are similar, though the Mariner 10 distribution is somewhat more extended towards higher albedos (highly reflective surface areas such as bright ray craters). Though two different hemispheres of Mercury are compared, the absence of such points in our present data set is likely an effect of seeing convolution as described above. This is verified by the presence of a number of well defined small bright spots (ray craters) on both hemispheres on better resolved ground-based image data (Warell & Limaye 2001). The implication is that the two studied hemispheres are very similar in their albedo–color properties, and presumably in the fractional areal distribution of known types of geologic units.

The VISNIR albedo–color distribution of Mercury has been mapped for a region overlapping that studied by Warell (2002). Though some pixel-to-pixel variations attributable to noise are apparent at spatial scales smaller than the seeing-smeared angular resolution, the maps (Fig. 5) show local multipixel regions with correlated brightness variations deviating from the mean or intermediate level, which we attribute to real variations on Mercury's surface. We note that the relative range of these variations is less than the case in the UVVIS (Fig. 4), which may imply that abundance variations in ferrous iron may be smaller than variations in opaque minerals at this spatial scale. The small VISNIR albedo and color variations are similar to those for the lunar farside (Fig. 3), suggesting that the surface is dominated by very mature regolith for which any originally strong mafic absorption bands have been reduced in contrast. The dominant geologic units are likely intercrater and smooth plains of predominantly low-iron and low-titanium feldspathic composition, as is the case for the Mariner 10 hemisphere (e.g., Rava & Hapke 1987; Blewett et al. 1997).
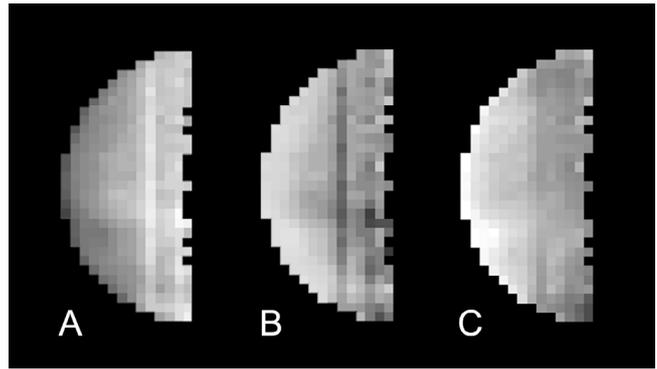

Fig. 5. Reduced VISNIR images of Mercury. Panel A displays the 950/750 nm ratio (range 1.21–1.40) which forms the basis for the derivation of the spectral parameters in the following two panels. Panel B shows the Fe-sensitive parameter θ_{Fe} (brighter indicates a higher iron abundance; pixel range 0.0–0.84), and panel C the optical maturity-sensitive OMAT parameter (bright features have a lower degree of optical maturity; pixel range 0.08–0.20).

In terms of color contrasts, Warell (2002) found no 940 nm/continuum-band contrast values >2% on better resolved but noisier data from parts of the presently studied hemisphere. Here too, the 950/750 nm ratio image (Fig. 5) displays low contrast, and the derived iron-sensitive and optical maturity images show small intensity variations from the average. We do however expect local to regional heterogeneities in the surface composition to be present (e.g., Rava & Hapke 1987; Robinson & Lucey 1997; Sprague et al. 2002; Blewett et al. 2005), and recently Warell et al. (2006) found such evidence in near infrared spectra of Mercury. We propose that the present maps verify that such local–regional variations in mafic mineralogy, detectable from ground-based data sets, exist on the mercurian surface. Intensity contrasts due to compositional heterogeneities, likely from low-iron minerals with varying transition metal cation abundances (Mg, Ca, Na, K, etc.), are probably more pronounced in the thermal infrared than in the optical–near infrared range due to the generally low iron and titanium content of the mercurian regolith (Mitchell & de Pater 1994; Jeanloz et al. 1995; Blewett et al. 1997a; Warell & Blewett 2004).

We find that features on the studied hemisphere of Mercury which are bright in reflectance are generally immature and have low to intermediate opaque mineral and intermediate abundances of ferrous iron. This is consistent with such features being bright immature ray systems of geologically young craters. The locations of the bright features are verified with the better-resolved data set of Warell & Limaye (2001). Thus we are in possession of a method of deriving the geologic natures of these high-reflectance regions, which is independent to the method with which such an identification was made by Warell & Limaye (2001).

The darkest areas in reflectance on Mercury's observed surface have intermediate maturities, intermediate to high opaque mineral abundances and intermediate ferrous iron abundances. These may correspond to localised regions of higher opaque abundances than the general mercurian surface (i.e., smooth plains and intercrater plains), perhaps derived by extrusive processes from crustal plutonic sources analogue to proposed source regions for the lunar maria (e.g., Head 1998).

Our results on the relative iron-maturity parameter and opaque index for the observed hemisphere may be compared with the findings by Robinson & Lucey (1997) based on Mariner 10 first encounter image data (longitudes 10–70°W). The least

opaque-rich and least mature formation in the latter data set is the Kuiper–Murasaki crater complex; pure number statistics based on the results presented here suggests that such features are more common in the 210–270°W longitude range (e.g., features #52, 53 and 55). Particularly interesting regions on the Mariner 10 hemisphere are the 500 km wide patch of blue material located northwest of the crater Lermontov, and the 250 km wide patch southwest of Homer. These display low maturities and high opaque contents which may be due to mafic material of pyroclastic origin (Robinson & Lucey 1997). We are not able to find units with such characteristics in the present dataset, which may be attributed to insufficient spatial resolution or contrast. One of our features, "B", does have a low maturity and a higher than average opaque content, but it is not bright in the 415/950 nm ratio image and is thus not likely a Kuiper–Murasaki-type crater.

One region in the present data set located at 245°W, 40°N (labelled "A" in Fig. 4) has a low opaque index but is otherwise not prominent in the reflectance or iron-plus-maturity maps. This signature is consistent with that of the extended 600 km wide region located west and south of the crater Rudaki (Robinson & Lucey 1997; Robinson & Taylor 2001), and those within the 160 km wide flooded craters Schubert, Petrarch and Ibsen on the Mariner 10 hemisphere. As suggested by Spudis & Guest (1988), these units may be low-iron basaltic material that has flooded the surface from below. They argue that Calorian epoch smooth plains are volcanic and may be similar to the lunar Apennine bench formation which is likely composed of extrusive basaltic lava higher in Al_2O_3 and lower in FeO than typical lunar mare basalts. The most probable composition of the average mercurian surface, $FeO+TiO_2 \leq 4\%$ (Jeanloz et al. 1995; Blewett et al. 1997, 2002; Warell & Blewett 2004) has less than half the iron and titanium content of the Apennine bench (Blewett et al. 1997). Jeanloz et al. (1995) argue that any mantle basalts that erupted to the surface were subject to extensive subcrustal or crustal differentiation, possibly yielding secondary eruptions that produce very alkaline extrusive lavas.

As for the coordinates of the points of origin in the equations of the titanium- and iron-sensitive parameters for the Moon, these are quantitatively correct only for the calibration of Clementine data carried out by Lucey et al. (2000a). The corresponding coordinates for Mercury derived here are thus unlikely to be quantitatively precise, irrespective of the intensity calibration and type of reflectance or albedo used, since the composition and importance of space weathering effects of the surfaces of the two bodies is different. Thus the derived spectral parameter maps are only interpretable in a qualitative sense, with respect to both intensity and scaling. With this caveat however, derived properties units on the observed surface of Mercury are directly comparable to each other.

Our scaling of the brightness of the Clementine 450 nm, 750 nm and 950 nm images relies on the average V-band geometric albedo for the integrated lunar nearside (Warell 2004) and the slope of the spectrum of a region in Mare Serenitatis for which Lucey et al. (2000a) published reflectance values at Clementine wavelengths. We note that the 750 nm albedo of the average global Moon derived here, and used in the comparison with the Mercury data, is fully consistent with results above derived from the integrated phase curves of the two bodies (Warell 2004).

Some issues of the photometric calibration of Clementine global image data (Eliason et al. 1999) were discussed by Hillier et al. (1999) and Shkuratov et al. (2000). They found a brightness difference between Clementine and Earth-based data, such that the Clementine calibration is about a factor two brighter. This effect was attributed to the fact that the Clementine data was absolutely scaled with laboratory reflectance measurements of lunar samples, while ground-based data was calibrated with visual photometry. Furthermore, Staid & Pieters (2000) noted that some Clementine spectra displayed an intensity "kink" between the 950 nm and 1000 nm filters which was suggested to be contributed by scattered light in the camera system. They also found non-systematic relative intensity variations in the UVVIS camera data resulting from variations in viewing geometry, and Kreslavsky et al. (2000) quantified the overall photometric precision to about 2%. These issues are unlikely to be important in the present analysis for several reasons. We calibrate the albedos of the two bodies with ground-based phase-curve data, the photometric precision of the Mercury data is likely not better than the Clementine calibration, and the calculation of the chemical and maturity parameters for Mercury is possible to interpret only qualitatively.

Comparison of TiO_2 abundance determinations based on Lunar Prospector neutron spectrometer data and derived with the Lucey method indicate that the latter underestimates abundances by several weight per cent in absolute or several hundred percent in a relative sense for mare regions with "anomalously" low reflectances and flat spectral continua (Gillis et al. 2001; Elphic et al. 2002; Shkuratov et al. 2005). The cause of this discrepancy is not known, but may be related to petrography (Gillis et al. 2001; Elphic et al. 2002). We do not know if similar effects occur on Mercury and we cannot presently address the issue. However, based on Mariner 10 imaging and ground-based data we do have reason to believe that optically dark and spectrally flat lava flow regions are less likely to be present on Mercury than on the Moon, as Mercury has a lower surface abundance of iron and a more mature surface (Cintala 1992; Mitchell & de Pater 1994; Jeanloz et al. 1995; Robinson & Lucey 1997; Warell & Limaye 2001; Warell & Blewett 2004). This fact reduces the likeliness that the TiO_2 abundance calibration discrepancy is important in the present analysis.

It is conceivable that the assumed mafic feldspar-rich model for the crustal composition (Rava & Hapke 1987), based on the observed properties of the lunar crust and surface, is not applicable to Mercury. The original silicate crust may have been removed by a surface volatilization process due to a hot early Sun (Fegley & Cameron 1987) or a giant impact (Wetherill 1987). In such a case, the present crust may lack substantial amounts of opaques (ilmenite), contain an large amount of ultramafic minerals (e.g., Ti-bearing clinopyroxenes) and be very low in Fe and Ti. The Charette et al. (1974) relation between Ti abundance and spectral reflectance is then no longer valid as substantial absorption may occur in strong allowed Fe^{2+}-Ti^{4+} charge-transfer bands centered at 340 and 420 nm. Small amounts of Ti would then cause a *reddening* of the spectrum, contrary to the assumption of the Lucey model (Hapke 2001). However, more volatile material of higher Fe and Ti abundance will likely have been provided to an original crust by late infall of meteoritic material, perhaps to such an extent as to partially disguise the chemical properties of an ultramafic crust formed from post-accretion loss of a substantial silicate component.

The geologic natures of features in the longitude range 210°–270° on Mercury's poorly known hemisphere that are suggested here are intriguing but more work needs to be done with multicolor image data of better resolution, higher signal-to-noise ratio, and global coverage. A key task would be to follow up with a similar study of ground-based data for the Mariner 10 hemisphere in particular, to achieve a direct comparison of

close range and ground-based data sets. This would allow a verification of the present results, a geochemical assessment of the global planet, as well as a comparison of the occurrence and distribution of the types of surface units on the well and poorly known hemispheres of Mercury, prior to the arrival of MESSENGER and BepiColombo.

6. Conclusions

1. The UVVIS albedo–color distribution of the presently observed section (longitudes 210°W–270°W) of Mercury's poorly known (i.e., unimaged by Mariner 10) hemisphere is very similar to that of the Mariner 10 incoming hemisphere (longitudes 10°W–70°W), which implies a similar fractional areal occurrence of known geologic units (intercrater plains, smooth plains, ray craters).

2. The small VISNIR albedo and color variations are similar to those for the lunar farside, suggesting that the surface is dominated by very mature surfaces for which any originally strong mafic absorption bands have been reduced to near detection limit for the present data set and spatial scale. The dominant geologic units are likely intercrater and smooth plains of predominantly low-iron and low-titanium feldspathic composition, as is the case on the Mariner 10 hemisphere.

3. The relative intensity range of spatial variations of spectral parameters in the VISNIR is less than the case in the UVVIS, which may imply that relative abundance variations in ferrous iron may be smaller than variations in opaque minerals at the 500 km spatial scale.

4. Highly reflective albedo features are generally immature, have low to intermediate abundances of opaque minerals and intermediate abundances of ferrous iron. This is consistent with such features being bright immature ray systems of geologically young craters.

5. The darkest areas in reflectance have intermediate maturities, intermediate to high opaque mineral abundances and intermediate ferrous iron abundances. These may correspond to localised regions of more opaque materials than is typical for the general mercurian surface, perhaps derived by local extrusive processes from crustal plutonic sources.

6. We show that ground-based high angular-resolution multi-color image data may be used with the Lucey method framework, originally developed from lunar remote sensing and geochemical data, to study the geologic natures of mercurian albedo features.

References

Blewett, D. T., Lucey, P. G., Hawke B. R., et al. 1997, Icarus, 129, 217
Blewett, D. T., Hawke, B. R., & Lucey, P. G. 2002, Meteorit. Planet. Sci., 37, 1245
Blewett, D. T., Hawke, B. R., Lucey, P. G. & Robinson, M. S. 2005, 36th Lunar Plan. Sci. Conf., abstract 1245
Bowell, E., Hapke, B., Domingue, D., et al. 1989, in Asteroids II, ed. R. Binzel, T. Gehrels, & M. S. Matthews (Tucson: U. Arizona Press), 525

Cassidy, W., & Hapke, B. 1975, Icarus, 25, 371
Charette, M. P., McCord, T. B., Pieters, C., & Adams, J. B. 1974, J. Geophys. Res., 79, 1605
Charette, M. P., Adams, J. B., Taylor, S. R., & McCord, T. B. 1977, 8th Lunar Sci. Conf., 1049
Cintala, M. J. 1992, J. Geophys. Res., 97, 947
Dollfus, A., & Auriere, M. 1974, Icarus, 23, 465
Domingue, D. L., Sprague, A. L., & Hunten, D. M. 1997, Icarus, 128, 75
Domingue, D., & Hapke, B. 1989, Icarus, 78, 330
Eliason, E., Isbell, C., Lee, E., et al. 1999. Mission to the Moon: The Clementine UVVIS Global Lunar Mosaic, PDS Volumes USA-NASA-PDS-CL-4001 through 4078 (U.S. Geological Survey), Planetary Data System
Elphic, R. C., Lawrence, D. J., Feldman, W. C., et al. 2002, J. Geophys. Res., 107, DOI 10.1029/2000JE001460
Emery, J. P., Sprague, A. L., Witteborn, F. C., et al. 1998, Icarus, 136, 104
Fegley, B., Jr., & Cameron, A. G. W. 1987, Earth Planet Sci. Lett., 82, 207
Gillis, J. J., Jolliff, B. L., Elphic, R. C., et al. 2001, 32nd Lunar Plan. Sci. Conf., 2185
Hapke, B., Cassidy, W., & Wells, E. 1975, Moon, 13, 339
Hapke, B. 2001, J. Geophys. Res., 106, 10 039
Hapke, B. 2002, Icarus, 157, 523
Head, J. W., III. 1998, in Workshop on New Views of the Moon: Integrated Remotely Sensed, Geophysical, and Sample Datasets, ed. B. L. Joliff & G. Ryder, 38
Hillier, J. K., Buratti, B. J., & Hill, K. 1999, Icarus, 141, 205
Isbell, C. E., Eliason, E., Adams, K. C., et al. 1999, 30th Lunar Planet Sci Conf., 1812
Jeanloz, R., Mitchell, D. L., Sprague, A. L. & de Pater, I. 1995, Science, 268, 1455
Keller, L., & McKay, D. 1997, Geochim. Cosmochim. Acta, 61, 2331
Kreslavsky, M. A., Shkuratov, Yu. G., Velikodsky, Yu. I., Kaydash, V. G., & Stankevich, D. G. 2000, J. Geophys. Res., 105, 20 281
Lucey, P. G., Blewett D. T., & Hawke, B. R. 1998, J. Geophys. Res., 103, 3679
Lucey, P. G., Blewett, D. T., & Joliff, B. L. 2000a, J. Geophys. Res., 105, 20 297
Lucey, P. G., Blewett, D. T., Taylor, G. J. & Hawke, B. R. 2000b, J. Geophys. Res., 105, 20 377
Mallama, A., Wang, D., & Howard, R. A. 2002, Icarus, 155, 253
Mitchell, D. L., & de Pater, I. 1994, Icarus, 110, 2
Morris, R. V. 1980, 11th Lunar Planet Sci Conf., 1697
Noble, S. K., Pieters, C. M., Taylor, L. A., et al. 2001, Met. Planet. Sci., 36, 31
Noble, S. K., & Pieters, C. M. 2003, Solar System Res., 37, 31
Pieters, C. M., Fischer, E. M., Rode, O., & Basu, A. 1993, J. Geophys. Res., 98, 20 817
Pieters, C. M., Taylor, L. A., Noble, S. K., et al. 2000, Met. Planet Sci., 32, 1101
Rava, B., & Hapke, B. 1987, Icarus, 71, 397
Robinson, M. S., & Lucey, P. G. 1997, Science, 275, 197
Robinson, M. S., & Taylor, G. J. 2001, Met. Planet Sci., 36, 841
Robinson, M. S., McEwen, A. S., Eliason, E., et al. 1999, 30th Lunar Planet Sci Conf., 1931
Sasaki, S., & Kurahashi, E. 2003, Adv. Space Res., 33, 2152
Shkuratov, Yu. G., Kaydash, V. G., Pieters, C., & Opanasenko, N. V. 2000, 31st Lunar Planet Sci. Conf., 1165
Shkuratov, Yu. G., Kaydash, V. G., Stankevich, D. G., et al. 2005, Plan. Space Sci., 53, 1287
Scharmer, G. B., Bjelksjö, K., Korhonen, T., Lindberg, B., & Pettersson, B. 2002, in Innovative Telescopes and Instrumentation for Solar Astrophysics, ed. S. Keil & S. Avakyan, Proc. SPIE, 4853
Sprague, A. L., Deutsch, L. K., Hora, J., et al. 2000, Icarus, 147, 421
Sprague, A. L., Emery, J. P., Donaldson, K. L., et al. 2002, Met. Planet. Sci., 37, 1255
Spudis, P. D., & Guest, J. E. 1988, in Mercury, ed. F. Vilas, C. R. Chapman, & M. S. Matthews (Tucson: U. Arizona Press), 118
Staid, M. I., & Pieters, C. M. 2000, Icarus, 145, 122
Taylor, L. A., Pieters, C. M., Keller, L. P., Morris, R. V., & McKay, D. S. 2001, J. Geophys. Res., 98, 27 985
Veverka, J., Helfenstein, P., Hapke, B., & Goguen, J. 1988, in Mercury, ed. F. Vilas, C. R. Chapman, & M. S. Matthews (Tucson: U. Arizona Press), 37
Warell, J. 2002, Icarus, 156, 303
Warell, J. 2003, Icarus, 161, 199
Warell, J. 2004, Icarus, 167, 271
Warell, J., & Blewett, D. T. 2004, Icarus, 168, 257
Warell, J., & Limaye, S. S. 2001, Plan. Space Sci., 49, 1531
Warell, J., Sprague, A. L., Emery, J., Kozlowski, R., & Long, A. 2006, Icarus, 180, 281
Wetherill, G. W. 1987, in Mercury, ed. F. Vilas, C. R. Chapman & M. S. Matthews (Tucson: U. Arizona Press), 670